Microscopic mechanism of low lattice thermal conductivity in natural superlattice materials BaXYF (X = Cu, Ag; Y = Se, Te) including fully quartic anharmonicity

Tongcai Yue,[1] Yinchang Zhao,[1,*] Jun Ni,[2,†] Sheng Meng,[3,4,‡] and Zhenhong Dai[1,§]

[1]*Department of Physics, Yantai University, Yantai 264005, People's Republic of China*

[2]*Department of Physics, Tsinghua University, Beijing 100084, People's Republic of China*

[3]*Beijing National Laboratory for Condensed Matter Physics and Institute of Physics, Chinese Academy of Sciences, Beijing 100190, People's Republic of China*

[4]*Collaborative Innovation Center of Quantum Matter, Beijing 100084, People's Republic of China*

(Received 4 July 2022; revised 21 October 2022; accepted 23 December 2022; published 9 January 2023)

Layered quaternary fluorochalcogenides with natural superlattice structures have received particular attention in the thermoelectric (TE) field due to their favorable electronic properties. However, further exploration of these materials in the TE field is hindered by the lack of studies on the lattice thermal transport properties. Here, we investigate the microscopic mechanism of lattice thermal transport in natural superlattice materials BaXYF (X = Cu, Ag; Y = Se, Te) using first-principles calculations combined with self-consistent phonon theory, compressive sensing techniques, and Boltzmann transport equations. We consider three- and four-phonon scattering as well as temperature-driven phonon energy shifts due to quartic anharmonicity. We find that the strong quartic anharmonicity plays a crucial role in the lattice stability of BaCuSeF and BaCuTeF. Furthermore, the κ_L of the four materials exhibits significant anisotropy due to different bonding types along the $a(b)$ and c axes. The calculations indicate that the four materials have low lattice thermal conductivities κ_L, e.g., 0.85–1.61 $Wm^{-1}K^{-1}$ at 300 K. Additionally, the results exhibit that a reasonable κ_L and corresponding temperature dependence can be obtained by considering the fully quartic anharmonicity. Our findings not only fill the gap in the lattice thermal transport research of natural superlattice materials, but also deepen a comprehensive understanding of the low κ_L of natural superlattice materials.

DOI: 10.1103/PhysRevB.107.024301

I. INTRODUCTION

Thermoelectric (TE) materials, which have the ability to directly convert heat into electricity, provide a feasible solution for alleviating the energy shortage and environmental pollution of energy use [1–4]. Generally, the TE conversion efficiency is measured by a dimensionless figure of merit $ZT = \frac{S^2\sigma T}{\kappa_e+\kappa_L}$, in which S, σ, κ_e, κ_L, and T are the thermopower, electrical conductivity, electrical thermal conductivity, lattice thermal conductivity, and absolute temperature, respectively. Among them, κ_L plays a crucial role in improving the TE conversion efficiency because it can even be reduced to the amorphous limit [5–7]. Recently, excellent TE properties have been reported in a series of layered materials, such as BiCuSeO [8], SnSe [9], and SnS [10], which is mainly attributed to the unique lattice structure, suggesting the relationship between complex bonding types, anisotropic transport properties, and strong lattice anharmonicity.

The quaternary ZrCuSiAs-type compounds are typical layered TE materials and have been extensively studied, especially BiCuSeO and its alloys, but BaXYF (X = Cu, Ag; Y = Se, Te) have not been extensively studied despite their large potential. Furthermore, these four compounds are also known as natural superlattice materials due to the lattice mismatch and electronic potential difference between the different layers. In particular, the near-two-dimensional electronic band structure [11,12] derived from the natural superlattice structure results in a large S. Concretely, the interlayer bonds along the stacking direction in natural superlattice materials are ionic bonds. The ionic character leads to a near-flat electronic structure, that is, the near-two-dimensional electronic band structure [13]. Furthermore, the near-flat electronic band structure leads to a large carrier effective mass and high electronic density of states, resulting in a large S [14]. Additionally, the lattice mismatch and unique bonding properties [15] lead to a strong anharmonicity. Moreover, BaXYF (X = Cu, Ag; Y = Se, Te) also have the advantages of lead-free, good thermal stability, abundant elements, low price, easy regulation, and feasible preparation scheme [16–18], which prompted us to conduct further research on its TE properties. Based on the first-principles calculations, Boudiaf and co-workers [11] and Sreeparvathy and co-workers [12] have predicted the possibility of excellent TE performance in the natural superlattice materials. However, the κ_L is estimated through Slack's equation [19], which usually overestimates the final results [20]. Moreover, they also lack deeper physical insight into the lattice thermal transport properties of the natural superlattice materials. Hence, this motivated us

*y.zhao@ytu.edu.cn
†junni@mail.tsinghua.edu.cn
‡smeng@iphy.ac.cn
§Corresponding author: zhdai@ytu.edu.cn

to investigate the microscopic mechanism of lattice thermal transport in four natural superlattice materials. Among them, the comprehensive understanding of BaCuSeF and BaCuTeF is hindered by challenges due to the imaginary frequencies of the phonon spectrum (lattice instabilities) of BaCuSeF and BaCuTeF [15], e.g., the calculations of Boltzmann transport equations (BTEs) based on harmonic approximations (HAs) is invalid for solving κ_{L} due to the existence of imaginary frequencies of the phonon spectrum.

In this paper, to solve the above problem, we investigate the lattice thermal transport properties of BaXYF (X = Cu, Ag; Y = Se, Te) using the state-of-the-art first-principles calculations scheme, which includes the effect of three-phonon (3ph) and four-phonon (4ph) scatterings on the phonon lifetimes τ_{ph} and the temperature-induced anharmonic renormalization of phonon frequencies arising from quartic anharmonicity in the four natural superlattice materials. Recent studies have indicated that the above first-principles calculations scheme is able to accurately reproduce experimental κ_{L} and the corresponding temperature dependence [21–23]. Our key findings are that even for these layered natural superlattice materials, the full inclusion of 3ph scattering, 4ph scattering, and quartic anharmonic renormalization of phonon frequencies are necessary to obtain rational κ_{L} and the corresponding temperature dependence, while the inclusion of only quartic anharmonic renormalization of phonon frequencies (4ph scattering) will lead to a higher (lower) κ_{L} and weaker (stronger) temperature dependence of κ_{L}. Furthermore, our results show that for the natural superlattice materials with weak quartic anharmonicity, e.g., BaAgSeF, $\kappa_{\mathrm{3ph}}^{\mathrm{HA}}$ could be accidentally consistent with $\kappa_{\mathrm{3,4ph}}^{\mathrm{SCP}}$ due to the error cancellation.

II. METHODOLOGY

To capture the lattice thermal transport properties in BaXYF (X = Cu, Ag; Y = Se, Te), we perform first-principles calculations with the projector-augmented wave method [24] and plane-wave basis set [25], implemented in the Vienna *ab initio* simulation package (VASP) [25–27]. We use 600 eV as the cutoff energy for the plane-wave basis set. The exchange-correlational interactions are simulated by the Perdew-Burke-Ernzerhof revised for solids (PBEsol) functional [28] of the generalized gradient approximation [29]. We use $14 \times 14 \times 8$ k-point samplings to fully optimize the unit cell until the total energy and forces' convergences are less than 10^{-8} eV and 10^{-4} eV/Å, respectively. To solve the nonanalytical part of the dynamics matrix, density functional perturbation theory (DFPT) [30] is used to capture the dielectric tensors and the Born effective charges. Furthermore, the electron localization function (ELF) is calculated to investigate the bonding properties of the four natural superlattice materials.

For the calculations of the HA and anharmonic interatomic force constants (IFCs), a $2 \times 2 \times 2$ supercell and $7 \times 7 \times 4$ **k** meshes are constructed, and the ALAMODE code [31,32] is used to extract second- to fourth-order IFCs. Concretely, the finite-displacement approach [33] is utilized to extract second-order IFCs from 10 configurations. To train the accurate cubic and quartic IFCs using compressive sensing lattice dynamics (CSLD) [34], one needs to extract the data set of displacements and forces from first-principles calculations in quasirandom configurations. It is intuitively attractive to use snapshot structures from *ab initio* molecular dynamics (AIMD) trajectories since these structures denote physically relevant low-energy configurations. Additionally, AIMD calculations can also generate physically relevant atomic displacements that are consistent with the nature of atomic bonding, closer to the real physical process. Hence, we first performed a AIMD simulation at 300 K for 4000 steps with a time step of 2 fs to obtain 80 snapshot structures, in which the canonical ensemble with the chosen Nosé mass controlling Nosé frequency of the temperature oscillations during the simulation, to be similar to the average phonon frequency, is used. Then, the desired quasirandom configurations used in first-principles calculations was obtained by adding displacements of 0.1 Å in random directions for each atom on the 80 snapshot structures. In the CSLD calculations, we include all nearest-neighbor interactions for IFCs, seventh- (fourth)-nearest-neighbor interactions for cubic (quartic) IFCs, and second-nearest-neighbor interactions for quintic and sextic IFCs. The self-consistent phonon (SCP) calculations are realized by utilizing the reciprocal-to-real-space Fourier interpolation, implemented in the ALAMODE code.

The phonon BTE is solved in $14 \times 14 \times 8$ k-point samplings, implemented in the FOURPHONON package [35–37]. The calculations capture about 10^7 3ph allowed processes and 1.1×10^{10} 4ph allowed processes. Based on the phonon BTE, the κ_{L} tensor is computed as

$$\kappa_{\mathrm{L}}^{\alpha\beta} = \frac{\hbar^2}{k_{\mathrm{B}} \mathrm{T}^2 \mathrm{V} N_q} \sum_{\mathbf{q}\nu} n_{\mathbf{q}\nu}(n_{\mathbf{q}\nu}+1)\omega_{\mathbf{q}\nu}^2 \upsilon_{\mathbf{q}\nu}^{\alpha} F_{\mathbf{q}\nu}^{\beta}, \tag{1}$$

where $\hbar$ is the reduced Planck's constant, k_{B} is the Boltzmann constant, V is the volume of the primitive cell, and N_q is the wave-vector number, respectively. $n_{\mathbf{q}\nu}$ and $\omega_{\mathbf{q}\nu}$ are the population and frequency of the phonon mode. $\mathbf{q}$ and ν specify the phonon mode $|\mathbf{q}\nu\rangle$. α and β specify the Cartesian directions. $\upsilon_{\mathbf{q}\nu}^{\alpha}$ is the phonon group velocity, and $F_{\mathbf{q}\nu}^{\beta}$ is written as

$$F_{\mathbf{q}\nu}^{\beta} = \tau_{\mathbf{q}\nu}\left(\upsilon_{\mathbf{q}\nu}^{\beta} + \Delta_{\mathbf{q}\nu}\right), \tag{2}$$

in which $\tau_{\mathbf{q}\nu}$ is the phonon lifetime under the single-mode relaxation time approximation (SMRTA), and $\Delta_{\mathbf{q}\nu}$ is the measure of deviates from the SMRTA prediction and is only available for iterative solutions of the BTE. The phonon BTE is solved in the iterative scheme for 3ph processes, but with 4ph processes computed by SMRTA due to the huge computational costs in the iterative solution of 4ph processes [37].

III. RESULTS AND DISCUSSION

The BaXYF (X = Cu, Ag; Y = Se, Te) crystallize in the ZrCuSiAs-type structure ($P4/nmm$ [129] space group) and have eight atoms in the unit cell, as shown in Figs. 1(a) and 1(b). The fluoritelike layers X_2Y_2 and antifluorite layers Ba_2F_2 are alternately stacked along the c axis to form a natural superlattice. The calculated lattice constants using the PBEsol functional for the four materials are listed in Table I, which are in good accordance with the experimental values [16–18]. Additionally, the ELF is calculated to capture the bonding

TABLE I. The calculated lattice constants a^{opt} and c^{opt} (in Å), total Grüneisen parameter γ^{total} [39], average κ_{L} (in $\text{Wm}^{-1}\text{K}^{-1}$) at 300 K, and temperature dependence of κ_{L} for the four natural superlattice materials BaCuSeF, BaCuTeF, BaAgSeF, and BaAgTeF. The averaged lattice thermal conductivities and corresponding temperature dependence are calculated using the HA + 3ph, HA + 3,4ph, SCP + 3ph, and SCP + 3,4ph, namely, $\kappa_{3\text{ph}}^{\text{HA}}$, $\kappa_{3,4\text{ph}}^{\text{HA}}$, $\kappa_{3\text{ph}}^{\text{SCP}}$, and $\kappa_{3,4\text{ph}}^{\text{SCP}}$. The experimental lattice constants a^{expt} and c^{expt} are listed for comparison.

Ba*XY*F	a^{opt}	a^{expt}	c^{opt}	c^{expt}	γ^{total}	$\kappa_{3\text{ph}}^{\text{HA}}$	$\kappa_{3,4\text{ph}}^{\text{HA}}$	$\kappa_{3\text{ph}}^{\text{SCP}}$	$\kappa_{3,4\text{ph}}^{\text{SCP}}$	$\kappa_{3\text{ph}}^{\text{HA}} \sim$	$\kappa_{3,4\text{ph}}^{\text{HA}} \sim$	$\kappa_{3\text{ph}}^{\text{SCP}} \sim$	$\kappa_{3,4\text{ph}}^{\text{SCP}} \sim$
BaCuSeF	4.19	4.239 [16]	9.10	9.122 [16]	1.833	0.77	0.54	2.82	1.61	$T^{-0.74}$	$T^{-1.04}$	$T^{-0.44}$	$T^{-0.66}$
BaCuTeF	4.38	4.4297 [17]	9.32	9.3706 [17]	1.620	0.86	0.35	2.06	1.09	$T^{-0.88}$	$T^{-1.13}$	$T^{-0.67}$	$T^{-0.99}$
BaAgSeF	4.32	4.3449 [18]	9.32	9.4018 [18]	1.866	1.42	0.78	2.16	1.42	$T^{-0.91}$	$T^{-1.18}$	$T^{-0.67}$	$T^{-0.90}$
BaAgTeF	4.50		9.52		1.854	0.76	0.37	1.50	0.85	$T^{-0.90}$	$T^{-1.26}$	$T^{-0.57}$	$T^{-0.83}$

properties of the four materials, as shown in Figs. 1(c)–1(e). Obviously, the electrons in the (100) plane are more delocalized compared to the (001) plane, indicating the weaker bond strength in the four materials along the c axis. The unique lattice structure with anisotropic bonding properties results not only in anisotropic electron transport properties [12], but is also expected to lead to anisotropy in the lattice thermal transport. Furthermore, the low-symmetry crystal structures easily lead to strong lattice anharmonicity due to the complex bonding types, which is beneficial to reduce the intrinsic κ_{L} of the materials.

Since the existence of strong lattice anharmonicity is a crucial role of many low-κ_{L} materials, it is necessary to study the lattice thermal transport behavior of the four natural superlattice materials as well as evaluate their lattice anharmonic strengths. In this paper, we first investigate the lattice vibrational properties of the four natural superlattice materials. The HA phonon dispersion of the four materials is plotted by the cyan lines in Fig. 2. Additionally, the first Brillouin zone and corresponding high-symmetry points are displayed in Fig. S6(a) in the Supplemental Material (SM) [39]. It can be observed that BaCuSeF and BaCuTeF have imaginary HA phonon frequencies, indicating lattice instabilities at 0 K. In contrast, BaAgSeF and BaAgTeF are dynamically stable at 0 K. Physically, the imaginary HA phonon frequencies are inconsistent with the experimentally observed stability of BaCuSeF and BaCuTeF at finite temperature, which indicate that HA approximations are invalid. The harmonic phonon density of states (HPDOS) reveal that the imaginary phonon frequencies are mainly contributed by the motions of Cu and Y atoms, as shown in Figs. 2(a) and 2(b). To further study the origin of lattice instability in BaCuSeF and BaCuTeF at 0 K, we also calculated the atomic motions of the lowest phonon branch at the Γ point for the four materials, as shown in Fig. S1 in the SM [39]. The opposite vibrations of inequivalent Cu and Te atoms at the Γ point in BaCuTeF lead to lattice instability at 0 K compared to the other three materials without imaginary frequencies at the Γ point. Concretely, the opposite vibrations of inequivalent atoms cause the distortion of the

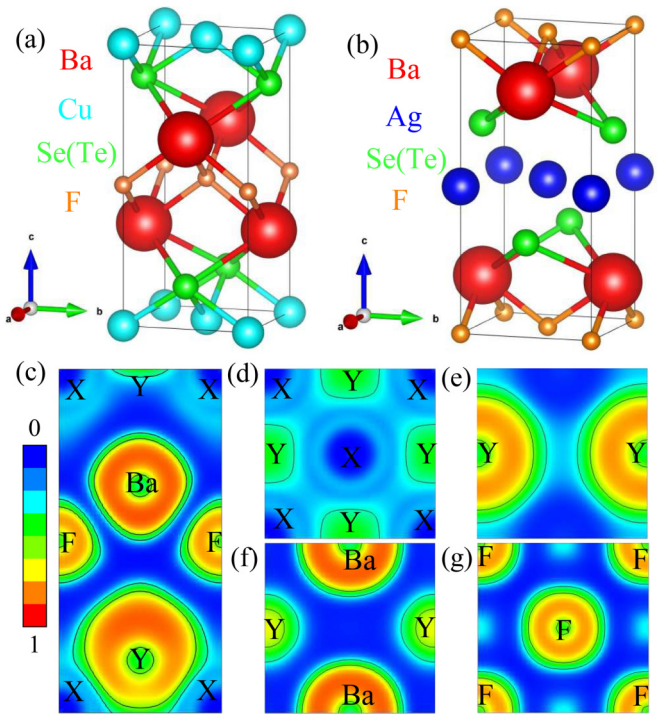

FIG. 1. The crystal structure of (a) BaCu*Y*F and (b) BaAg*Y*F (Y = Se, Te). Electron localization function (ELF) of Ba*XY*F (X = Cu, Ag; Y = Se, Te) in the (c) (100) plane and (d)–(g) (001) plane, where 1 denotes completely localized electrons while 0 denotes fully delocalized electrons. The distances from the origin are (c) 0 Å in the (100) plane, (d) 0, (e) 1.37, (f) 2.97, and (g) 4.55 Å in the (001) plane. The above crystal structure and ELF are visualized in the VESTA code [38].

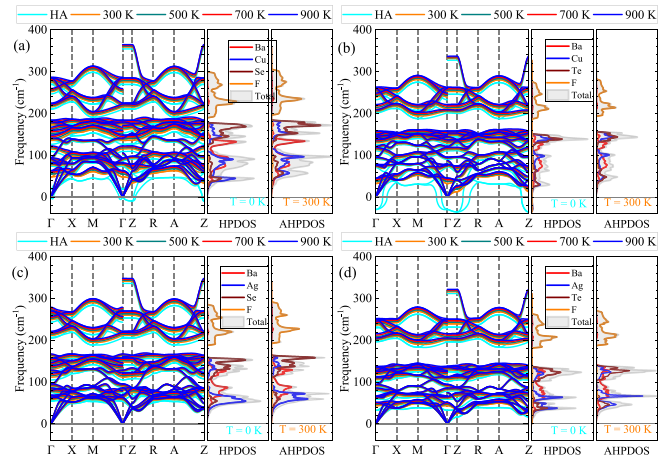

FIG. 2. Calculated temperature-dependent phonon spectrum from T = 0 to 900 K and corresponding projected phonon density of states (PDOS) at T = 0 and 300 K for (a) BaCuSeF, (b) BaCuTeF, (c) BaAgSeF, and (d) BaAgTeF. The 0 K represents the result of the HA approximations.

Cu_2Te_2 layer, resulting in the lattice instability of BaCuTeF at 0 K. The above analysis reveals that the anharmonic effects should have significantly large displacement amplitudes to counteract the distortion of the lattice structure.

Motivated by this point, we next investigated the impact of quartic anharmonicity on the phonon frequencies ω_{ph}. Figure 2 displays the anharmonic phonon dispersion from $T =$ 300 to 900 K for the four materials, which indicate an obvious hardening of the low-lying phonon modes below 80 cm^{-1} with the increasing temperature. These phonon modes are mainly contributed by the vibrations of the X and Y atoms, as revealed by the anharmonic phonon density of states (AHP-DOS) at 300 K in Fig. 2. Additionally, these high-lying optical phonon modes relevant to the majority of the F atoms motions are also moderately hardened. Among them, the phonon frequencies of the X atoms exhibit small values, but display strong temperature dependence. The interesting vibrational behavior associated with X atoms is similar to the rattling behavior in the cage structure, which is expected to bring about strong lattice anharmonicity and low κ_L. This phenomenon is exacerbated by large mean-square displacements (MSDs) at 300 K (see Fig. S2 in the SM [39]) and weak bonding strength of the X atoms. Furthermore, because of the strong phonon modes' hardening arising from strong quartic anharmonicity, no imaginary phonon frequencies are observed in BaCuSeF and BaCuTeF, suggesting that the quartic anharmonic effect is crucial for the lattice stability of these two materials.

In the following, we compared the magnitudes of the quartic anharmonic renormalization of the phonon frequencies of the four materials. Evidently, the hardening of low-lying phonon frequencies is more pronounced as the atomic number of X decreases and atomic number of Y increases. From the phonon density of states (PDOS) in Fig. 2, it can be seen that the hardening of the phonon frequencies is mainly due to the enhancement of the quartic anharmonicity of the X atoms. Concretely, as the atomic number of X decreases, X atoms have larger displacement amplitudes due to their lighter atomic mass, resulting in stronger anharmonicity. Additionally, as the atomic number of Y increases, the electronegativity of Y atoms decreases, resulting in the weaker bonding strength around the X atoms. The coexistence of larger displacement amplitudes and looser bonding of the Cu atoms leads to stronger lattice anharmonicity in BaCuTeF. Furthermore, as shown in Fig. S2 in the SM [39], we see that the Cu atoms in BaCuTeF have the largest MSD; the value is 0.025 $Å^2$ along the $a(b)$ axis at 300 K. In contrast, the MSD of the Ag atoms in BaAgSeF are the smallest, with a value of only 0.017 $Å^2$ along the $a(b)$ axis at $T = 300$ K. The calculated MSDs further confirmed our above analysis, e.g., Cu atoms have larger displacement amplitudes.

As shown in Eq. (1), in addition to the ω_{ph}, the phonon group velocity υ_{ph} and the phonon lifetime τ_{ph} are also key components of the phonon BTE. Hence, we continue to investigate lattice thermal transport properties of the four natural superlattice materials by researching how the quartic anharmonicity affects υ_{ph} and τ_{ph}. Figure 3 shows the calculated υ_{ph} by using HA approximations and SCP approximations, which reveals a significant increase in the υ_{ph} of low- and high-frequency phonon modes with increasing temperature. Since BaCuSeF and BaCuTeF have imaginary HA phonon

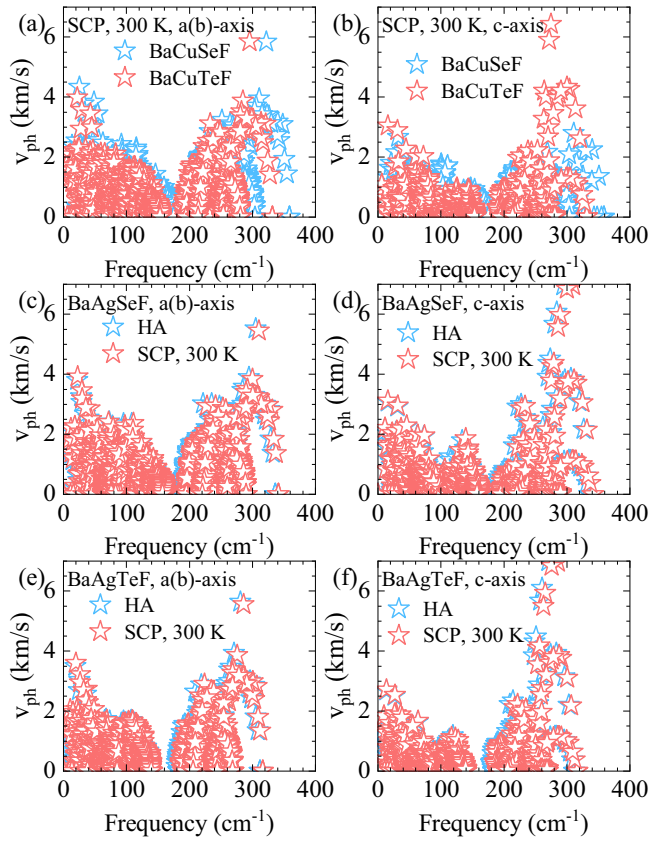

FIG. 3. The calculated phonon group velocity υ_{ph} for BaCuSeF, BaCuTeF, BaAgSeF, and BaAgTeF computed in HA approximations and SCP approximations, respectively.

frequencies, the solutions to phonon BTE are numerically invalid. Hence, only the thermal transport parameters calculated based on the SCP approximations are provided in BaCuSeF and BaCuTeF. Additionally, compared with BaAgSeF, the υ_{ph} of BaAgTeF increases more obviously with the increase of temperature, which is consistent with the stronger quartic anharmonicity of BaAgTeF. Furthermore, as the mass of the X and Y atoms increases, the phonon frequencies decrease, resulting in a decrease in the υ_{ph}. The κ_L of BaAgTeF is expected to be the lowest among the four natural superlattice materials as the decrease in the υ_{ph}. Similarly, the lower κ_L along the c axis can be captured in the four natural superlattice materials because of the lower υ_{ph} along the c axis than that along the $a(b)$ axis. The lower υ_{ph} along the c axis can be attributed to the softening of the low-frequency phonon dispersion in the Γ-Z direction due to the weaker bonding strength along the c axis, as shown in Fig. 2. Interestingly, the high-frequency phonon modes contributed by the F atoms have an unusually larger υ_{ph} along the c axis, which can be attributed to the stronger bonding strength of the F atoms along the c axis than along $a(b)$ axis, as shown in Figs. 1(b) and 1(g). Additionally, the differences in υ_{ph} along the different directions is also the main reason for the anisotropic of phonon thermal transport properties in the four natural superlattice materials. The anisotropic in κ_L can be used to established directional heat transport in nanoelectronic devices [40]. Furthermore, we can also achieve anisotropic

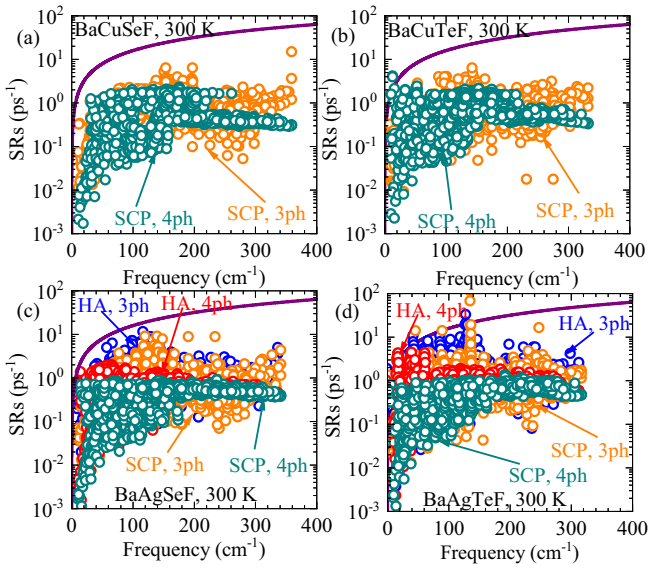

FIG. 4. Comparison of 3ph scattering rates (SRs) calculated in HA approximations (blue circles) and SCP approximations (orange circles), and 4ph SRs calculated in HA approximations (red circles) and SCP approximations (dark cyan circles), for (a) BaCuSeF, (b) BaCuTeF, (c) BaAgSeF, and (d) BaAgTeF along the $a(b)$ axis and c axis, respectively.

modulation of phonon thermal transport through nanostructures [41].

Moreover, the phonon lifetime τ_{ph} also play a crucial role in the phonon BTE. Hence, we next investigated the effect of quartic anharmonicity on the τ_{ph}. To verify the validity of the phonon quasiparticle picture [42,43], we also display $1/\tau_{ph} = \omega_{ph}/2\pi$ by purple solid lines in Fig. 4. When $1/\tau_{ph} < \omega_{ph}/2\pi$ is not satisfied, it means that the phonon annihilates before completing one vibrational cycle, and the phonon in the quasiparticle picture is invalid. Figure 4 shows that almost all 3ph and 4ph scattering rates (SRs) are distributed under the curve of $1/\tau_{ph} = \omega_{ph}/2\pi$, which confirms the validity of the phonon BTE. As shown in Fig. 4, 3ph and 4ph SRs decrease significantly with the hardening of the phonon frequencies, which can ultimately be attributed to the suppressed Grüneisen parameter γ and scattering phase space (see Fig. S3 in the SM [39]) [44,45]. Strikingly, in the low-frequency phonon modes, the 4ph scattering processes can reach or even exceed the 3ph scattering processes, which is consistent with the more pronounced phonon frequencies hardening in the low-frequency phonon modes. The large 4ph SRs also indicate that the quartic anharmonicity is non-negligible in the lattice thermal transport of the four natural superlattice materials.

Furthermore, the 3ph SRs increase with the atomic masses of X and Y, which can be traced back to the large 3ph scattering phase space caused by narrower phonon dispersion. Concretely, the phonon dispersion narrows with increasing atomic masses of X and Y, leading to an increase in the 3ph scattering processes satisfying the conservation of momentum and energy. Additionally, we observe that the γ increases with increasing X atomic number and decreasing Y atomic number. γ is usually used to characterize the strength 3ph scattering. The increased γ also means that the τ_{ph} decreases gradually as the atomic number of X increases and the atomic number of Y decreases. For a more intuitive comparison, the total γ of the four materials at 300 K are also listed in Table I. After careful studies, we found that the quartic anharmonic renormalization of the phonon frequencies significantly suppressed the γ. Actually, the 3ph SRs are determined by both the γ and 3ph scattering phase space. The above analysis indicates that for these four natural superlattice materials, the contribution of the 3ph scattering phase space to the 3ph SRs is more significant. Additionally, we also compared the 4ph scattering intensities of the four natural superlattice materials computed by SCP approximations. As in our previous analysis, 4ph SRs exhibit a similar trend to phonon frequency hardening, i.e., 4ph SRs increase with decreasing X atomic number and increasing Y atomic number. In contrast, the 4ph scattering phase space increases with increasing X and Y atomic number, as shown in Figs. S3(c)–S3(h) in the SM [39]. The effect of 4ph scattering phase spaces and the quartic anharmonic strength on the 4ph SRs compete with each other. The calculations show that the 4ph scattering phase space is more competitive in the 4ph SRs.

To better understand the 3ph and 4ph scattering processes, the mode-resolved 3ph and 4ph SRs at 300 K are shown in Fig. S4 in the SM [39]. For 3ph scattering processes, we consider splitting ($\lambda \rightarrow \lambda' + \lambda''$) and combination ($\lambda + \lambda' \rightarrow \lambda''$) processes by using the SCP approximations at 300 K, in which λ denotes the phonon mode $|\mathbf{q}\nu\rangle$. Evidently, the combination processes in low-frequency (high-frequency) phonon modes are superior (inferior) to the splitting processes, which can be explained by the mode-resolved 3ph scattering phase spaces. Because of the constraints of energy conservation and momentum conservation in the scattering processes, low-frequency phonon modes are likely to combine to form high-frequency phonon modes, while high-frequency phonon modes are inclined to split into low-frequency phonon modes, as shown in Figs. S5(a), S5(c), S5(e), and S5(g) in the SM [39]. Additionally, the combination processes also take precedence over the splitting processes at 180 to 220 cm^{-1} due to the existence of the phonon band gap, especially for BaAgTeF. Moreover, for 4ph scattering, we include the splitting ($\lambda \rightarrow \lambda' + \lambda'' + \lambda'''$), redistribution ($\lambda + \lambda' \rightarrow \lambda'' + \lambda'''$), and recombination ($\lambda + \lambda' + \lambda'' \rightarrow \lambda'''$) processes. Since the redistribution processes are more likely to satisfy momentum and energy conservation, both the 4ph scattering phase spaces and SRs are dominated by the phonon redistribution processes, as shown in Figs. S4 and S5 in the SM [39]. Furthermore, the splitting and recombination processes of 4ph scattering exhibit the same trend as the splitting and combination processes of 3ph scattering, e.g., the recombination (splitting) processes are more related to the low-frequency (high-frequency) phonon modes, as shown in Figs. S4 and S5 in the SM [39]. Meanwhile, we also include normal and Umklapp processes for 4ph scattering, as plotted in Figs. S4(c), S4(f), S4(i), and S4(l) in the SM [39]. Normal processes do not directly create thermal resistance, but play a crucial role in redistributing momentum among phonons, while Umklapp processes provide thermal resistance and impede the movement of phonons [46]. The Umklapp processes are superior to the normal ones in the four materials, suggesting that the 4ph scattering processes are primarily due to the reduction

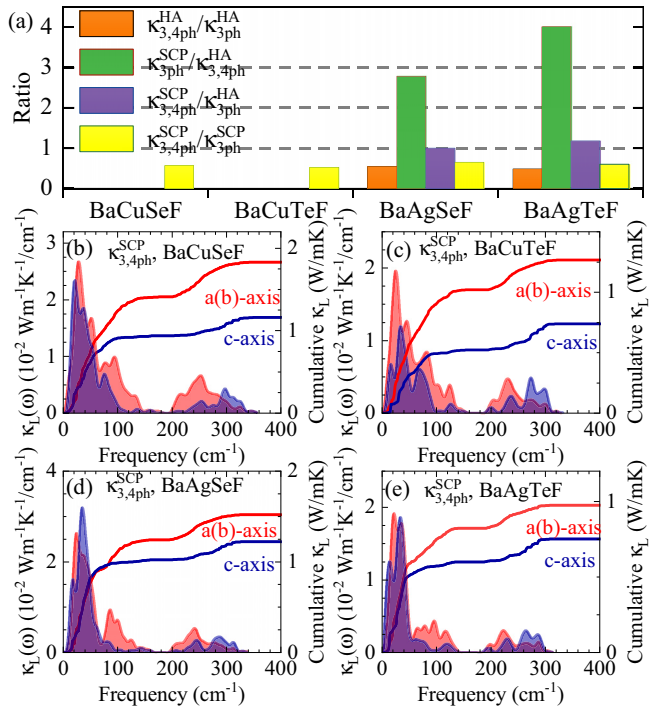

FIG. 5. (a) The ratios of $\kappa^{HA}_{3,4ph}/\kappa^{HA}_{3ph}$, $\kappa^{SCP}_{3ph}/\kappa^{HA}_{3ph}$, $\kappa^{SCP}_{3,4ph}/\kappa^{HA}_{3ph}$, and $\kappa^{SCP}_{3,4ph}/\kappa^{SCP}_{3ph}$ at 300 K for the four natural superlattice materials. Comparison of phonon frequency cumulative (solids lines) and differential (filled area below the curves) $\kappa^{SCP}_{3,4ph}$ for (a) BaCuSeF, (b) BaCuTeF, (c) BaAgSeF, and (d) BaAgTeF along the $a(b)$ axis and c axis, respectively.

in κ_L due to thermal resistance rather than the momentum redistribution of phonons.

To uncover the effects of the quartic anharmonicity from many aspects, the phonon frequency cumulative and differential κ_L are calculated, as shown in Figs. 5(b)–5(e) and Figs. S6(b)–S6(i) in the SM [39]. We found that the phonon modes below 140 cm^{-1} contribute more than 70% of κ_L. It can be observed that the major contributions to the decreased (increased) κ_L calculated with HA + 3,4ph (SCP + 3ph) relative to HA + 3ph mainly originate from the phonon frequency below 80 cm^{-1}, which is consistent with their large 4ph SRs (significantly increased υ_{ph} and reduced 3ph SRs). Additionally, the κ_L calculated with SCP + 3,4ph are significantly enhanced in low-frequency phonon modes relative to HA + 3ph, which reveals that the quartic anharmonic renormalization of low-lying phonon frequencies has a greater effect on the κ_L. In contrast, the high-frequency phonon modes are dominated by 4ph scattering, manifesting as a significant reduction in the κ_L of the high-frequency phonon modes. In the following, we compared the differential κ_L of the four natural superlattice materials computed with SCP + 3,4ph along the $a(b)$ and c axes, respectively. As shown in Figs. 5(b)–5(e), the κ_L contributed by midfrequency phonon modes along the c axis exhibit lower values, which can be attributed to the small υ_{ph} (see Fig. 3) and large phonon SRs (see Fig. 4) caused by the narrow phonon dispersion in the Γ-Z direction. Additionally, because of the larger υ_{ph} at high-frequency phonon modes along the c axis, the κ_L of high-frequency phonon modes along the c axis is higher than the $a(b)$ axis. For a more intuitive comparison, we superimpose the calculated phonon frequency cumulative lattice thermal conductivities under different approximations on the same plot, as shown in Fig. S10 in the SM [39].

Based on the effective lattice thermal transport parameters, we calculated the temperature-dependent lattice thermal conductivities κ^{HA}_{3ph}, $\kappa^{HA}_{3,4ph}$, κ^{SCP}_{3ph}, and $\kappa^{SCP}_{3,4ph}$ for the four natural superlattice materials, respectively. We start to compare the κ_L calculated by four different levels of theory, as plotted in Fig. 6. When the HA + 3ph is improved by including the quartic anharmonic renormalization of phonon frequencies (SCP + 3ph), the κ_L increased significantly, consistent with their remarkably increased υ_{ph} and reduced 3ph SRs. In contrast, the κ_L decrease remarkably when the additional 4ph scattering (HA + 3,4ph) is considered based on the HA + 3 ph. Additionally, there are moderate increases in κ_L for the four materials when the HA + 3ph is improved by including the fully quartic anharmonicity (SCP + 3,4ph), which is in agreement with the more pronounced quartic anharmonic renormalization of phonon frequencies. Recently, Xia [43,45] and Zhao [21] *et al.* have demonstrated that experimental κ_L and the corresponding temperature dependence in strongly anharmonic materials such as PbTe, Tl_3VSe_4, and perovskites can be reproduced considering the full quartic anharmonicity. Moreover, because of the smaller υ_{ph} along the c axis, the lower κ_L along the c axis for the four materials are observed in Fig. 6.

Furthermore, since the experimentally observed κ_L are generally isotropic, we also plot the average κ_L. As in our previous analysis, as the atomic mass increases, the average κ_L decreases because of increased SRs and reduced υ_{ph}. To quantitative analysis, the averaged κ_L at 300 K are also listed in Table I. Interestingly, the average $\kappa^{SCP}_{3,4ph}$ in BaAgSeF is almost in agreement with the average κ^{HA}_{3ph} at 300 K, which can be attributed to error cancellation [45,47]. In our previous analysis, the quartic anharmonicity of BaAgSeF was the weakest. Hence, for natural superlattice materials with weak quartic anharmonicity, the reasonable κ_L can be captured even without considering the quartic anharmonicity, avoiding the huge computational costs of 4ph scattering. The maximum average $\kappa^{SCP}_{3,4ph}$ of these four materials at 300 K is only 1.61 $Wm^{-1}K^{-1}$, which is much lower than that of the classical TE material PbTe [48,49]. Meanwhile, the low κ_L also means that the four natural superlattice materials have greater application potential in thermal management and TE fields. Generally, if the density of states of the imaginary phonon modes is small, rational κ_L can be obtained by ignoring the imaginary phonon frequencies. Hence, we also calculated the κ_L of BaCuSeF and BaCuTeF based on HA approximations, as shown in Fig. 6. The κ^{HA}_{3ph} and $\kappa^{HA}_{3,4ph}$ of BaCuSeF and BaCuTeF at 300 K and the corresponding temperature dependence are also listed in Table I. Interestingly, the κ^{HA}_{3ph} in BaCuSeF is much lower than that of $\kappa^{SCP}_{3,4ph}$. Further analysis revealed that the imaginary phonon modes lead to softening of the low-lying phonon branches, resulting in larger 3ph and 4ph SRs, as shown in Figs. S12(a) and S12(b) in the SM [39]. Additionally, the υ_{ph} calculated by HA approximations is almost the same as that calculated by

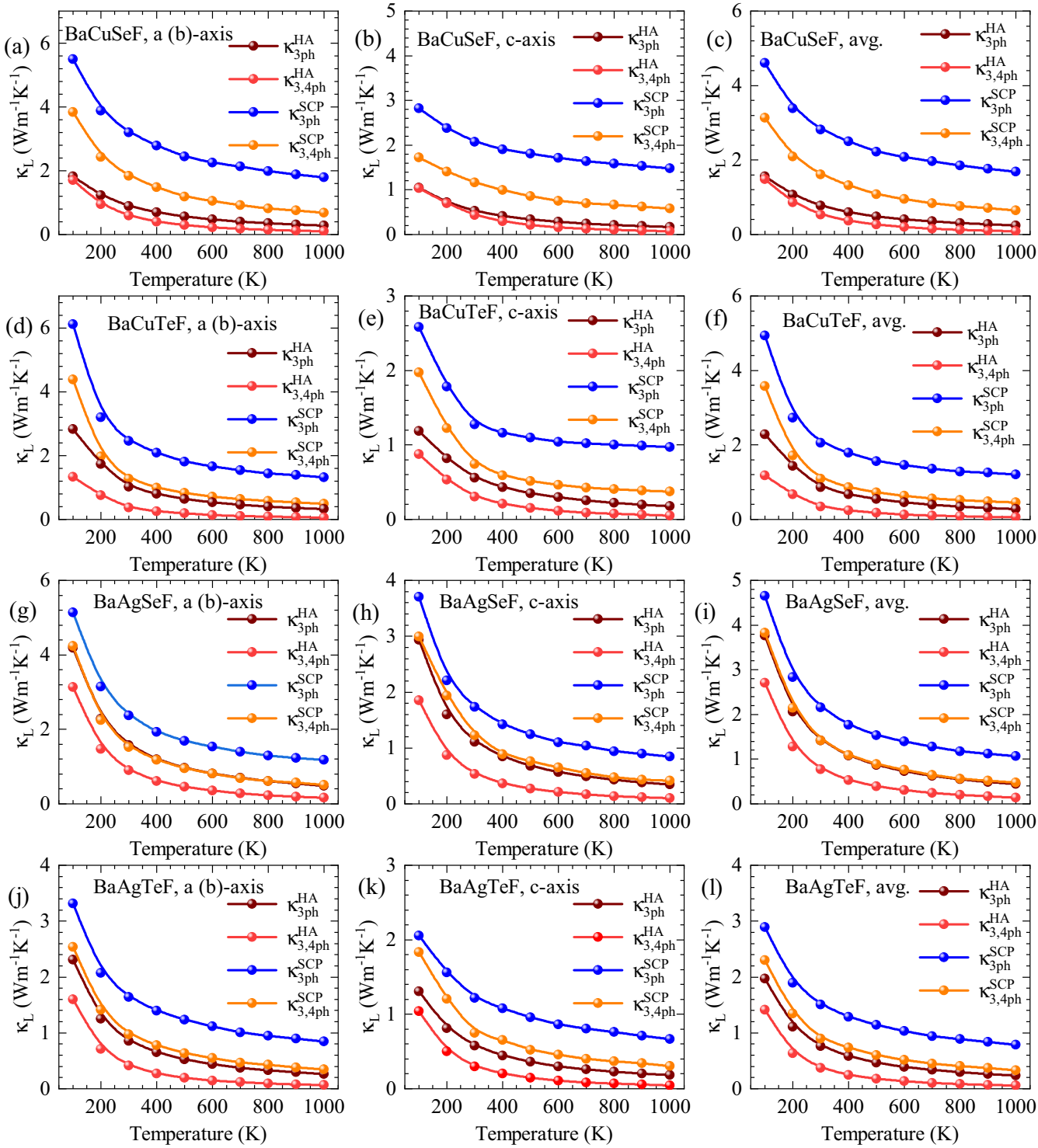

FIG. 6. The temperature-dependent lattice thermal conductivities κ_{3ph}^{HA}, $\kappa_{3,4ph}^{HA}$, κ_{3ph}^{SCP}, and $\kappa_{3,4ph}^{SCP}$ calculated using four levels of theory for (a)–(c) BaCuSeF, (d)–(f) BaCuTeF, (g)–(i) BaAgSeF, and (j)–(l) BaAgTeF. The left, middle, and right plots represent the κ_L of the $a(b)$ axis, c axis, and average, respectively.

SCP approximations. The above results show that although the small imaginary phonon modes of BaCuSeF have little effect on υ_{ph}, they can cause significant changes in SRs and thus lead to inappropriate κ_L. On the other hand, the values of κ_{3ph}^{HA} of BaCuTeF are closer to $\kappa_{3,4ph}^{SCP}$. Figure S11(c) in the SM [39] indicated that the large low-frequency HA υ_{ph} is responsible for the above results. However, the larger υ_{ph} is unreasonable due to the sharp softening of imaginary phonon modes. Hence, the κ_L of BaCuSeF and BaCuTeF calculated by HA approximations are problematic.

To further investigate the physical mechanism of lattice thermal transport of the four natural superlattice materials,

we give the temperature dependence of the averaged κ_L, which is described by the power law of $\kappa_L \sim T^{-\theta}$, as listed in Table I. When the HA + 3ph is improved by including only 4ph scattering processes (quartic anharmonic renormalization of phonon frequencies), the higher- (lower)-temperature dependence of the κ_L is captured. The higher-(lower)-temperature dependence of κ_L deviates significantly from T^{-1}, indicating that the results are overestimated (underestimated). When the HA + 3ph is improved by including the full quartic anharmonicity (SCP + 3,4ph), the rational temperature dependence of the κ_L can be captured in the four natural superlattice materials, as listed in Table I. Among them, BaCuTeF exhibits the stronger temperature dependence of κ_L due to its stronger anharmonicity. Furthermore, like κ_L, the temperature dependence of $\kappa^{SCP}_{3,4ph}$ is almost the same as κ^{HA}_{3ph} in BaAgSeF because of error cancellation. The result further validates our above conclusion that for weakly anharmonic materials, even without considering higher-order anharmonic effects, a reasonable lattice thermal transport information can be captured due to the error cancellation. Notably, the phonon frequencies are also affected by additional phonon softening mechanisms, such as thermal expansion at finite temperature. If the thermal expansion at finite temperature is incorporated into lattice thermal transport, then κ_L and the temperature dependence of κ_L will have better overall agreement with experiments.

Furthermore, we provide the ratios of $\kappa^{HA}_{3,4ph}/\kappa^{HA}_{3ph}$, $\kappa^{SCP}_{3ph}/\kappa^{HA}_{3ph}$, $\kappa^{SCP}_{3,4ph}/\kappa^{HA}_{3ph}$, and $\kappa^{SCP}_{3,4ph}/\kappa^{SCP}_{3ph}$ at 300 K, as plotted in Fig. 5(a). Among them, the value of $\kappa^{HA}_{3,4ph}/\kappa^{HA}_{3ph}$ indicates the additional 4ph scattering processes computed in HA approximations, the ratio of $\kappa^{SCP}_{3ph}/\kappa^{HA}_{3ph}$ reveals the influence of quartic anharmonic renormalization of phonon frequencies calculated in SCP approximations, and the result of $\kappa^{SCP}_{3,4ph}/\kappa^{HA}_{3ph}$ reflects the net influence of fully quartic anharmonicity. Particularly, $\kappa^{SCP}_{3,4ph}/\kappa^{SCP}_{3ph}$ and $\kappa^{HA}_{3,4ph}/\kappa^{HA}_{3ph}$ have similar information, i.e., both represent the relative change in κ_L due to the additional 4ph scattering processes. However, $\kappa^{HA}_{3,4ph}/\kappa^{HA}_{3ph}$ is invalid when applied to materials with imaginary HA phonon frequencies. Additionally, $\kappa^{HA}_{3,4ph}/\kappa^{HA}_{3ph}$ is insufficient to describe the additional 4ph scattering when applied to materials with strong anharmonicity because temperature-driven phonon energy shifts caused by strong quartic anharmonicity also affect the 4ph scattering phase spaces [42,43]. Hence, $\kappa^{SCP}_{3,4ph}/\kappa^{SCP}_{3ph}$ can be applied in whole natural superlattice materials, including the structure with imaginary HA phonon frequencies and strong quartic anharmonicity. As the quartic anharmonicity increases, the values of $\kappa^{SCP}_{3,4ph}/\kappa^{SCP}_{3ph}$ decrease for the four materials, indicating enhanced 4ph scattering. Additionally, $\kappa^{SCP}_{3,4ph}/\kappa^{SCP}_{3ph}$ of the four materials exhibit low values (0.53–0.66), which further indicates that 4ph SRs is comparable with the 3ph SRs. Likewise, we can infer that the quartic anharmonic renormalization of phonon frequencies also has a greater influence on the four materials. As displayed in Fig. 4(a), with $\kappa^{SCP}_{3ph}/\kappa^{HA}_{3ph}$ having large ratios, the values >2.5 for BaAgSeF and BaAgTeF. Due to the suppression of 4ph scattering phase space, $\kappa^{SCP}_{3,4ph}/\kappa^{SCP}_{3ph}$ has a small value relative to $\kappa^{HA}_{3,4ph}/\kappa^{HA}_{3ph}$ for BaAgSeF and BaAgTeF. Actually, there are competing behaviors for the influences of the quartic anharmonic renormalization of phonon frequencies and 4ph scatterings on the κ_L. Hence, the net influence of fully quartic anharmonicity is crucial. Due to stronger anharmonicity, the $\kappa^{SCP}_{3,4ph}/\kappa^{HA}_{3ph}$ is greater than 1 in BaAgTeF, which indicates that 4ph interactions increase κ_L in BaAgTeF. In contrast, because of cancellation of errors, the $\kappa^{SCP}_{3,4ph}/\kappa^{HA}_{3ph} \sim 1$ in BaAgSeF with weaker anharmonicity. The above results indicate that for more anharmonic systems, it is crucial to consider the full quartic anharmonicity, as they are less likely to benefit from error cancellation. For comparison, we also perform a third-order SMRTA calculation to quantify the difference produced by the iterative solution, as shown in Fig. S13 in the SM [39]. Interestingly, we also observed the phenomenon of error cancellation in SMRTA results, i.e., the $\kappa^{SCP}_{3,4ph}/\kappa^{HA}_{3ph} \sim 1$ in BaAgSeF. The above results reconfirm our conclusion that for materials with weak quartic anharmonicity, $\kappa^{SCP}_{3,4ph}$ is rational due to error cancellation.

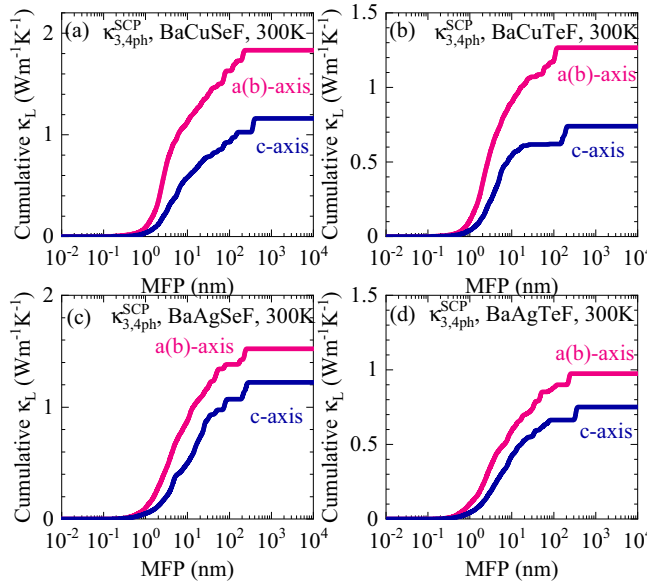

FIG. 7. The mean free paths cumulative $\kappa^{SCP}_{3,4ph}$ at 300 K for (a) BaCuSeF, (b) BaCuTeF, (c) BaAgSeF, and (d) BaAgTeF along the $a(b)$ axis and c axis, respectively.

To assess the potential to reduce κ_L through nanostructuring, we study the maximum mean-free-path (MFP) cumulative κ_L calculated in SCP + 3,4ph, as shown in Fig. 7. It can be observed that heat carriers (phonon) have large MFPs with the maximum values of about 210, 110, 240, and 240 nm for BaCuSeF, BaCuTeF, BaAgSeF, and BaAgTeF along the $a(b)$ axis at 300 K, respectively. Meanwhile, the maximum MFPs is 380, 200, 260, 310 nm for BaCuSeF, BaCuTeF, BaAgSeF, and BaAgTeF along the c axis at 300 K, respectively. The phonon quasiparticle picture indicates that the low κ_L can be captured through nanostructuring. If the maximum MFP is constrained to 10 nm, the κ_L of BaAgTeF along the c axis at 300 K can even be reduced to 0.48 Wm^{-1}K^{-1}. Additionally, the κ_L of BaCuSeF along the $a(b)$ axis can also be reduced to 1.30 m^{-1}K^{-1}. The low κ_L indicates that these four natural superlattice materials BaXYF (X = Cu, Ag; Y = Se, Te) are expected to have broad application prospects in the thermal management and TE fields.

IV. CONCLUSION

In summary, we have systematically investigated the lattice thermal transport properties in four natural superlattice materials, BaXYF (X = Cu, Ag; Y = Se, Te), by using the state-of-the-art first-principles calculations scheme, which includes the effects of quartic anharmonic renormalization of phonon frequencies and 4ph scattering. The calculations indicate that the metal atoms X exhibit strong quartic anharmonicity because of its large MSD and loose bonding strength, and stabilize BaCuSeF and BaCuTeF at finite temperature. Additionally, the 4ph SRs of the four natural superlattice materials exhibit anomalously large values in the low-frequency phonon modes, even comparable to the 3ph SRs, and play an important role in lattice thermal transport. Due to the coexistence of small υ_{ph} and strong lattice anharmonicity, the κ_{L} in the four natural superlattice materials are remarkably low, much lower than that of the classical TE material PbTe. Meanwhile, because of weaker bonding strength along the c axis, these four materials have lower κ_{L} along the c axis. Furthermore, our calculations indicate that reasonable κ_{L} and the corresponding temperature dependence of four natural superlattice materials can be obtained by additionally considering quartic anharmonic renormalization of phonon frequencies and 4ph scattering on the basis of HA + 3ph. Our studies unveil the microscopic mechanism of low κ_{L} in natural superlattice materials BaXYF (X = Cu, Ag; Y = Se, Te) and recommend them as potential thermal management and TE materials.

ACKNOWLEDGMENTS

This research were supported by the National Natural Science Foundation of China under Grants No. 11974302 and No. 12174327, and the Graduate Innovation Foundation of Yantai University, GIFYTU under Grant No. KGIFYTU2213.

[1] J. R. Sootsman, D. Y. Chung, and M. G. Kanatzidis, Angew. Chem., Int. Ed. **48**, 8616 (2009).
[2] T. Yue, Y. Sun, Y. Zhao, S. Meng, and Z. Dai, Phys. Rev. B **105**, 054305 (2022).
[3] Y. Zhao, C. Lian, S. Zeng, Z. Dai, S. Meng, and J. Ni, Phys. Rev. B **102**, 094314 (2020).
[4] T. M. Tritt, Annu. Rev. Mater. Res. **41**, 433 (2011).
[5] T. Yue, B. Xu, Y. Zhao, S. Meng, and Z. Dai, Phys. Chem. Chem. Phys. **24**, 4666 (2022).
[6] P.-C. Wei, C.-N. Liao, H.-J. Wu, D. Yang, J. He, G. V. Biesold-McGee, S. Liang, W.-T. Yen, X. Tang, J.-W. Yeh, Z. Lin, and J.-H. He, Adv. Mater. **32**, 1906457 (2020).
[7] L. Wang, M. Hong, Q. Sun, Y. Wang, L. Yue, S. Zheng, J. Zou, and Z.-G. Chen, ACS Appl. Mater. Interfaces **12**, 36370 (2020).
[8] L.-D. Zhao, J. He, D. Berardan, Y. Lin, J.-F. Li, C.-W. Nan, and N. Dragoe, Energy Environ. Sci. **7**, 2900 (2014).
[9] L. Su, D. Wang, S. Wang, B. Qin, Y. Wang, Y. Qin, Y. Jin, C. Chang, and L.-D. Zhao, Science **375**, 1385 (2022).
[10] R. Guo, X. Wang, Y. Kuang, and B. Huang, Phys. Rev. B **92**, 115202 (2015).
[11] K. Boudiaf, A. Bouhemadou, Y. Al-Douri, R. Khenata, S. Bin-Omran, and N. Guechi, J. Alloys Compd. **759**, 32 (2018).
[12] P. Sreeparvathy and V. Kanchana, J. Phys. Chem. Solids **111**, 54 (2017).
[13] V. K. Gudelli, V. Kanchana, G. Vaitheeswaran, D. J. Singh, A. Svane, N. E. Christensen, and S. D. Mahanti, Phys. Rev. B **92**, 045206 (2015).
[14] Y. Pei, A. D. LaLonde, H. Wang, and G. J. Snyder, Energy Environ. Sci. **5**, 7963 (2012).
[15] J. He, Y. Xia, W. Lin, K. Pal, Y. Zhu, M. G. Kanatzidis, and C. Wolverton, Adv. Funct. Mater. **32**, 2108532 (2022).
[16] H. Yanagi, J. Tate, S. Park, C.-H. Park, D. A. Keszler, M. Hirano, and H. Hosono, J. Appl. Phys. **100**, 083705 (2006).
[17] C.-H. Park, R. Kykyneshi, A. Yokochi, J. Tate, and D. A. Keszler, J. Solid State Chem. **180**, 1672 (2007).
[18] D. O. Charkin, A. V. Urmanov, and S. M. Kazakov, J. Alloys Compd. **516**, 134 (2012).
[19] G. Slack, J. Phys. Chem. Solids **34**, 321 (1973).
[20] R. Juneja, G. Yumnam, S. Satsangi, and A. K. Singh, Chem. Mater. **31**, 5145 (2019).
[21] Y. Zhao, S. Zeng, G. Li, C. Lian, Z. Dai, S. Meng, and J. Ni, Phys. Rev. B **104**, 224304 (2021).
[22] N. K. Ravichandran and D. Broido, Phys. Rev. B **98**, 085205 (2018).
[23] Y. Xia and M. K. Y. Chan, Appl. Phys. Lett. **113**, 193902 (2018).
[24] P. E. Blöchl, Phys. Rev. B **50**, 17953 (1994).
[25] G. Kresse and J. Furthmüller, Phys. Rev. B **54**, 11169 (1996).
[26] G. Kresse and J. Furthmller, Comput. Mater. Sci. **6**, 15 (1996).
[27] G. Kresse and J. Hafner, Phys. Rev. B **49**, 14251 (1994).
[28] G. I. Csonka, J. P. Perdew, A. Ruzsinszky, P. H. T. Philipsen, S. Lebègue, J. Paier, O. A. Vydrov, and J. G. Ángyán, Phys. Rev. B **79**, 155107 (2009).
[29] J. P. Perdew, K. Burke, and M. Ernzerhof, Phys. Rev. Lett. **77**, 3865 (1996).
[30] S. Baroni, S. de Gironcoli, A. Dal Corso, and P. Giannozzi, Rev. Mod. Phys. **73**, 515 (2001).
[31] T. Tadano and S. Tsuneyuki, Phys. Rev. B **92**, 054301 (2015).
[32] T. Tadano, Y. Gohda, and S. Tsuneyuki, J. Phys.: Condens. Matter **26**, 225402 (2014).
[33] K. Esfarjani and H. T. Stokes, Phys. Rev. B **77**, 144112 (2008).
[34] F. Zhou, B. Sadigh, D. Åberg, Y. Xia, and V. Ozoliņš, Phys. Rev. B **100**, 184309 (2019).
[35] T. Feng, L. Lindsay, and X. Ruan, Phys. Rev. B **96**, 161201 (2017).
[36] T. Feng and X. Ruan, Phys. Rev. B **93**, 045202 (2016).
[37] Z. Han, X. Yang, W. Li, T. Feng, and X. Ruan, Comput. Phys. Commun. **270**, 108179 (2022).
[38] K. Momma and F. Izumi, J. Appl. Crystallogr. **41**, 653 (2008).
[39] See Supplemental Material at http://link.aps.org/supplemental/10.1103/PhysRevB.107.024301 for the vibration modes in the lowest phonon branch, as well as the temperature-dependent atomic mean-square displacements, comparison of Grüneisen

parameter γ calculated in the SCP and HA approximations, decomposed 3ph scattering rates, decomposed 3ph scattering phase spaces, and phonon frequency cumulative and differential κ_L

[40] M. Zeraati, S. M. Vaez Allaei, I. Abdolhosseini Sarsari, M. Pourfath, and D. Donadio, Phys. Rev. B **93**, 085424 (2016).

[41] Y. Zeng and A. Marconnet, Phys. Rev. Appl. **9**, 011001 (2018).

[42] T. Yue, P. Sui, Y. Zhao, J. Ni, S. Meng, and Z. Dai, Phys. Rev. B **105**, 184304 (2022).

[43] Y. Xia, K. Pal, J. He, V. Ozoliņš, and C. Wolverton, Phys. Rev. Lett. **124**, 065901 (2020).

[44] T. Tadano and S. Tsuneyuki, Phys. Rev. Lett. **120**, 105901 (2018).

[45] Y. Xia, Appl. Phys. Lett. **113**, 073901 (2018).

[46] S. Shin, Q. Wang, J. Luo, and R. Chen, Adv. Funct. Mater. **30**, 1904815 (2020).

[47] Y. Xia, V. I. Hegde, K. Pal, X. Hua, D. Gaines, S. Patel, J. He, M. Aykol, and C. Wolverton, Phys. Rev. X **10**, 041029 (2020).

[48] G. Bagieva, G. Murtuzov, G. Abdinova, E. Allakhverdiev, and D. S. Abdinov, Inorg. Mater. **48**, 789 (2012).

[49] A. El-Sharkawy, A. E.-A. AM, M. Kenawy, A. Hillal, and H. Abu-Basha, Int. J. Thermophys. **4**, 261 (1983).